JJMIE

Volume 16, Number 5, December. 2022
ISSN 1995-6665
Pages 865– 878

Jordan Journal of Mechanical and Industrial Engineering

Study on the Impact of Sawtooth Roof Inclination Angles and Asymmetrical Opening Positions for An Isolated Building in Cross Ventilation

Osamah Hashem Al-Aghbari [a], Lip Kean Moey [b, *], Vin Cent Tai [b], Tze Fong Go[c], Mohammad Hossein Yazdi [d]

[a] *Faculty of Engineering, Built Environment & Information Technology, SEGi University, Selangor, Malaysia*

[b] *Centre for Modelling and Simulation, Faculty of Engineering, Built Environment & Information Technology, SEGi University, Selangor, Malaysia*

[c] *Centre for Advance Materials and Intelligent Manufacturing, Faculty of Engineering, Built Environment & Information Technology, SEGi University, Selangor, Malaysia*

[d] *New Materials Technology and Processing Research Center, Department of Mechanical Engineering, Neyshabur Branch, Islamic Azad University, Neyshabur, Iran*

Received 9 Aug 2022 *Accepted 21 Aug 2022*

Abstract

The opening configurations and roof inclination angles are important to determine the effectiveness of wind driven cross ventilation within building. This study presents Computational Fluid Dynamics (CFD) simulations to analyse the natural ventilation flow in a generic isolated building with four opening configurations which are bottom-top, bottom-middle, middle-top and middle-middle. The sawtooth roof was considered with different inclination angle of 9°, 18° and 27°. The 3-D Steady Reynolds Averaged Navier Stokes (RANS) equations were solved with the shear stress transport k-ω turbulence model. Based on the simulation results, the roof configuration and roof inclination angles highly affect the airflow characteristics within the building. Additionally, the various opening positions strongly influence the indoor airflow. Whenever the roof inclination angle is increased, the indoor airflow velocity increases due to the pressure difference between the windward and leeward openings within the building. Meanwhile, the highest pressure coefficient is obtained for the middle-top opening position with the lower roof inclination angle of 9°. Furthermore, increasing in roof inclination angle up to 27° leads to reduce pressure coefficient due to the increasing of internal velocity. The highest volume flow rate (VFR) across all simulation cases is found to be the middle-top opening position with the roof inclined angle of 27°. This occurs because the roof inclination angle of 27° is the geometry with the largest leeward height, which increases the volume flow rate. Therefore, increasing the roof inclination angle with the leeward opening near the roof leads to increase in better volume flow rate for the building.

Keywords: Computational Fluid Dynamics (CFD), Sawtooth Roof, Roof Inclination Angles (RIA), Opening Positions, Volume flow Rate (VFR).

1. Introduction

Natural ventilation is a passive design method for bringing cold air into a building that is typically warmer than the outside. It is possible to minimize power consumption for buildings by 10-30% with suitable building roof design and natural ventilation strategies [1]. The design of building openings can aid in ensuring a suitable ventilation circuit between incoming and exiting air flow [2]. However, the advent of air conditioners in the 1960s as well as the development of mechanical ventilation systems in buildings place a strain on the global energy consumption. According to Marina et al. the energy utilized by commercial buildings amounts for a whopping 32% of overall energy consumption globally [3]. Additionally, Hassan et al. discovered that buildings in Malaysia consumed nearly half of the electricity produced in the country, with commercial buildings using up to 39 kGWh [4]. The majority of the energy provided to buildings is used for air conditioners, which cool down offices and provide thermal comfort to the occupants. Carbon dioxide emissions through conventional energy sources such as fossil fuels used to supply the ever-increasing demand for electricity contribute to global warming [5]. As a result, carbon dioxide emissions of buildings have increased over the years. Behari estimates that the world will become 1.5°C warmer between 2030

* Corresponding author e-mail: moeylipkean@segi.edu.my.

and 2052, which could lead to extreme weather conditions and stronger heat waves [6]. Renewable energy sources such as wind can offer important environmental, social and economic benefits [7, 8].

There are different types of roofs which include hip, venturi, gable and sawtooth configurations [9]. Lim et al. examined various design parameters such as tower height variations, tower shapes, rooftop tilt angles, and various roof shapes for a naturally ventilated wind tower to determine the extraction air flow rate and airflow pattern. The results showed that the biconcave shape tower helps to enhance the venturi effect with the constriction at its cross section, resulting in a low pressure zone with an increase in air velocity extracted. The effect of increasing the roof tilt angle showed a higher angle of attack on the airflow and helped increase the extraction rate whereby the 45° tilt angle was the best among all cases investigated [10]. Moey et al. performed a study on the effect of venturi shaped roof on the air change rate (ACH) for a stairwell. The study was carried out through a wind tunnel study and a numerical simulation. The simulation results showed that when the roof angle increased from 20°- 60°, an increase in ACH was obtained [11]. Furthermore, Moey et al. conducted a numerical study using CFD simulation to investigate the effect of saltbox roof and gable roof configurations on wind induced natural ventilation for an isolated building with various roof pitches of 15°, 25°, 35° and 45°. The results showed that the saltbox roof configuration exhibit better performance than gable roof based on the measured parameters [12]. On the other hand, Tominaga et al. performed CFD simulations and wind tunnel experiments to investigate the airflow patterns around an isolated gable roof building with varying inclination angles. The result indicated that the roof pitches influence the flow field along with the streamline, turbulent kinetic energy distribution and pressure coefficient spatial distribution around and over the building [13]. Liu et al. studied the exterior airflow surrounding buildings with various type of roofs, such as flat roof, gable roof and stepped roof. The large eddy simulations (LES) were applied in the current study. The simulation findings revealed that the roof design has a significant impact on velocity, flow pattern and streamline distribution near buildings particularly at the pedestrian level [14].

The sawtooth roof for buildings has the potential to improve sustainability and healthy indoor environment by allowing more natural ventilation compared to the basic flat roof. The sawtooth roof can produce consistent and higher intensity level of air by locating the opening near the roof rather than the opening at the center or bottom of the façade [15]. The sawtooth roof can be implemented in several types of buildings, such as hospitals, low rise residentials and universities [16, 17]. Peren et al. performed CFD simulations to investigate the effect of the outlet opening positions and the sawtooth roof inclination angles on a natural ventilated building design. This study confirmed that sawtooth roof inclined angle effect the dimensionless velocity magnitude, pressure coefficient, and dimensionless streamwise wind speed ratio around the building. The numerical result showed an increase in roof inclination angle above 18° resulted in a significantly higher air flow rate. The roof including a 45° slant was the best-case scenario. Similarly, positioning the outlet opening closer to the roof was proved to be preferable, as it boosted the flow rate about 25% [18]. Therefore, it is important to examine the impact of asymmetrical opening positions at both windward and leeward with roof inclination angle as this affects the volume flow rate and airflow pattern of a naturally ventilated building [18]. However, to the best of authors' knowledge, the study on the influence of sawtooth roof inclination angles in conjunction with asymmetric positions of windward and leeward openings for the building has not been thoroughly investigated in the literature. Hence, the focus of this study is to investigate the effect of sawtooth roof inclination angles (RIA) and asymmetrical opening positions at both windward and leeward for a generic isolated building in cross ventilation.

The model dimensions, computational setup, boundary condition, solver settings and grid sensitivity analysis are described in Section 2. The simulation cases of sawtooth roof with four opening positions and various roof inclination angle (RIA) are presented in Section 3. Section 4 presents the CFD simulation results of sawtooth roof building with the opening positions and the impact of roof inclination angles and opening positions on airflow pattern, pressure coefficient and volume flow rate. Lastly, Section 5 concludes the simulation findings of this paper.

2. CFD Simulation: Model and Computational Setup

2.1. Building Geometry Model

In the current study, the reference model used was based on the wind induced cross ventilation of a generic isolated building by Karava et al. [19]. This reference model has a reduced scale of 1:200 and with the dimensions of $0.1\ m \times 0.1\ m \times 0.08\ m$ $(L \times W \times H)$. The reference model has two asymmetric openings which the windward opening is at the lower end of the windward façade at h = 0.02 m (from the ground to the window center) and the leeward opening at the upper end of the leeward façade h = 0.06 m. The windows opening dimensions were $0.046\ m \times 0.018\ m$ $(L \times H)$. In addition, the reference building model's wall thickness remains uniform among all surfaces at $0.002\ m$ [20]. Furthermore, the building model for simulation cases were constructed by determining a trapezoid height of sawtooth roof (increasing leeward height and reducing windward façade) along with different roof inclination angles (RIA), and different opening positions. More information on the simulation cases will be discussed in section 3. ANSYS 2021 R2 Space-Claim was used to generate the model's geometry. Figure 1 illustrates the roof inclination angle of 9° isometric view and side view.

2.2. Computational Flow domain and Grids

Based on the building geometry specified in the previous section, the computational flow domain can be generated. The isometric view of the flow domain is shown in Figure 2a while the front and side view of the domain are shown in Figure 2b and Figure 2c, respectively. The flow domain within the named selection zones such as symmetry, inlet, outlet, side wall, top wall

and ground is illustrated in Figure 2a. Additionally, the body of influnce (BOI) around the building was created and named as near-field BOI. The near BOI was generated by an offset of 1H or $0.08\,m$ from both sides, windward and leeward as illistruted in Figure 2b.

Next, in terms of the flow domain design specifications, the distance from the building to the sides of the flow domain was 5H whereby H is the building height of $0.08\,m$ [21–23]. Adding up to that, the distance from the leeward side of the building to the outlet plane of the flow domain is specified at 15H to ensure the flow is developed [24]. Meanwhile, the distance of windward façade of the building upstream to the inlet plane is set at 3H to control the occurrence of unintended streamwise gradients in the approach-flow profile. Overall, the flow domain design was set based on the CFD guidelines [20, 24, 25].

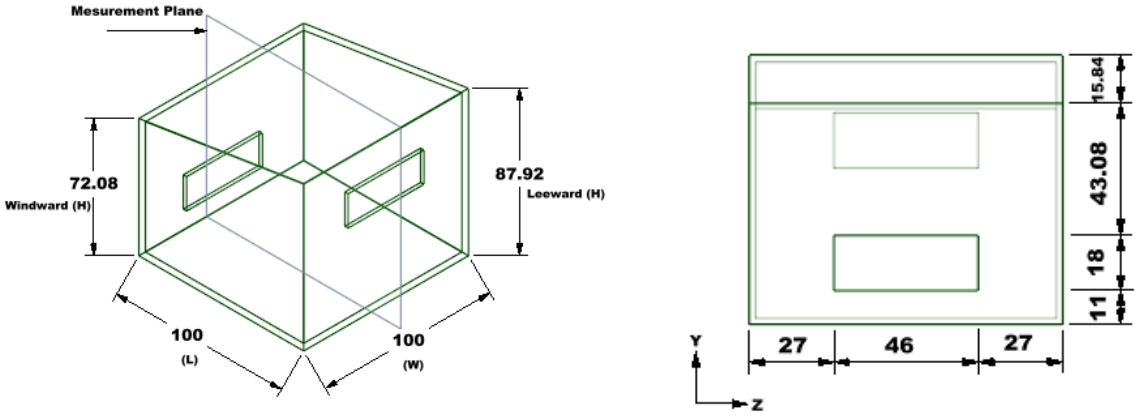

(a) (b)

Figure 1. Reduced scale of sawtooth roof building model (a) RIA-9° isometric view and (b) RIA-9° side view of bottom-top opening position.

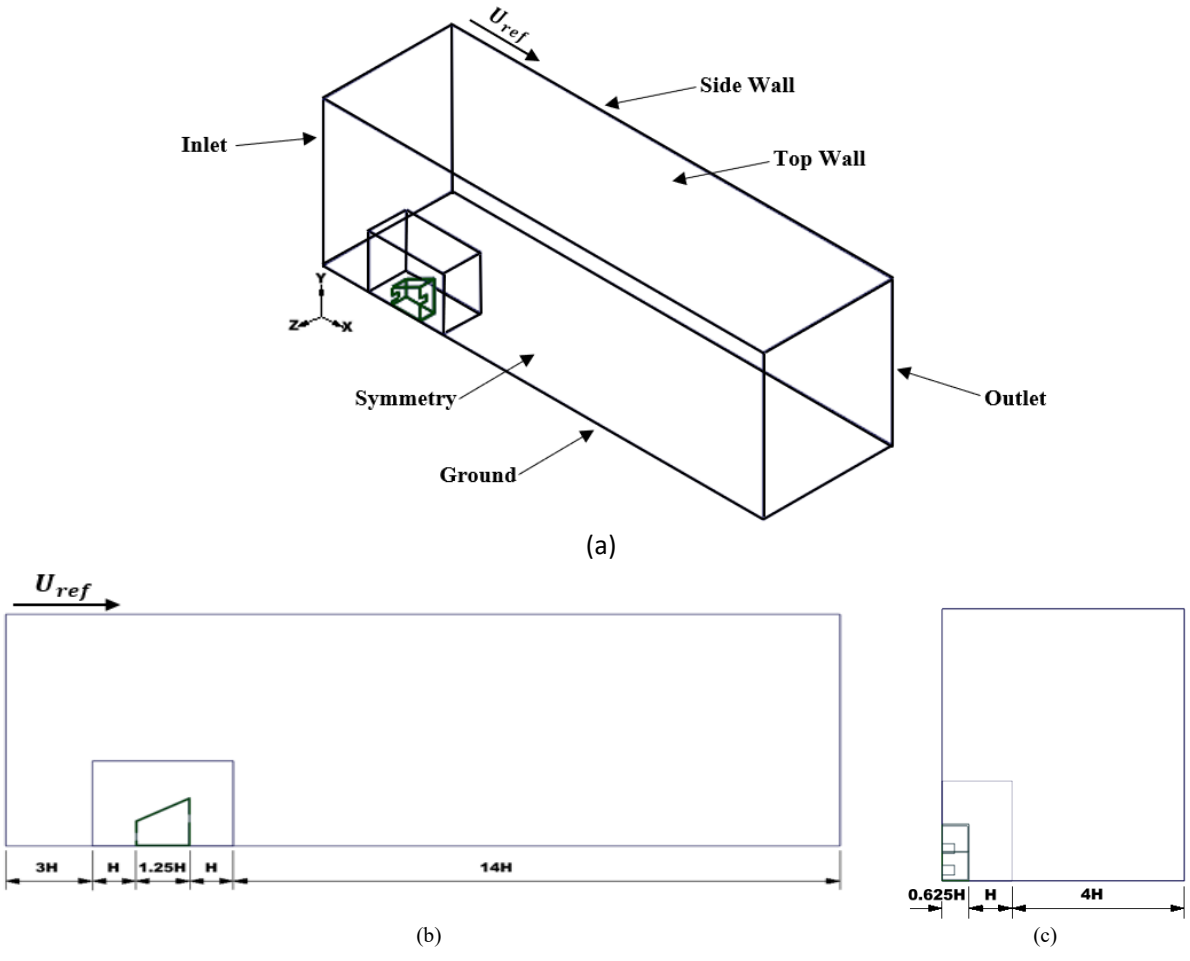

Figure 2. Computational flow domain (a) isometric view (b) front view and (c) side view.

Through using finite element approach, the meshing procedure describes the process of separating or splitting the geometry of the design across millions of uniformly dispersed parts defined as elements and nodes [26]. Fluent meshing from Ansys 2021 R2 [27] was used to produce the volume mesh as one of the pre-processing levels. After the design was constructed, the meshing procedure was carried out using the Watertight Meshing method. Furthermore, the building model was surounded by a body of influnce (BOI) with a size of $0.08\,m \times 0.08\,m \times 0.08\,m$ $(L \times W \times H)$ as 1H from the building sides as well as top and bottom, so that minimize computational time and enhancing precision of the findings by improving the mesh throughout this region, as recommended from the literture [12]. As a result, the body of influnce and the building model were surounded by the flow domain, and the mesh sizing has been accomplished by adjusting the global and local scoping size. Since the building under consideration is a generic design, a bluff body having sharp edges, flow separation at the rooftop of the building was unavoidable, particularly with such a high Reynolds number around 38K, which indicating a turbulent flow. The building was indeed subjected to proximity sizing in order to refine existing meshes around the building's edges. Whenever the local sizing was performed, the global scope sizing was applied towards the surface mesh. The surface mesh growth rate was fixed to 1.2 to help ease the transition from the flow domain approaching the entire building [13]. Next, as depict in Figure 3, the volume mesh was implemented after the surface mesh. Figure 4 shows a poly-hexcore volume mesh containing 10 uniformly prismatic layers surrounding the building. According to Zore et al. [28], the benefit of implementing Poly-hexcore grid is it reduces simulation time about 10-40% while reducing cell count by 20-40%. Furthermore, the Poly-hexcore meshes contains polyhedral elements throughout the transition area, octree hexahedral elements mostly in bulk region, as well as layered premium quality iso poly-inflations inside the boundaries layer, as recommended from the literature [28]. The first cell height utilized was $0.0001\,m$, as indicated throughout the preliminary calculations based on the a y+ of 3 and 10 inflation layers. A normal curvature angle of 12 degrees and two cells per gap have been established. Finally, the goal cell quality limit was set around 0.2-0.3, resulting in an inversely orthogonal quality (skewness) of 0.3, which is regarded as a good quality. Furthermore, the average skewness was 0.45, that belongs within an excellent range of cells quality [29].

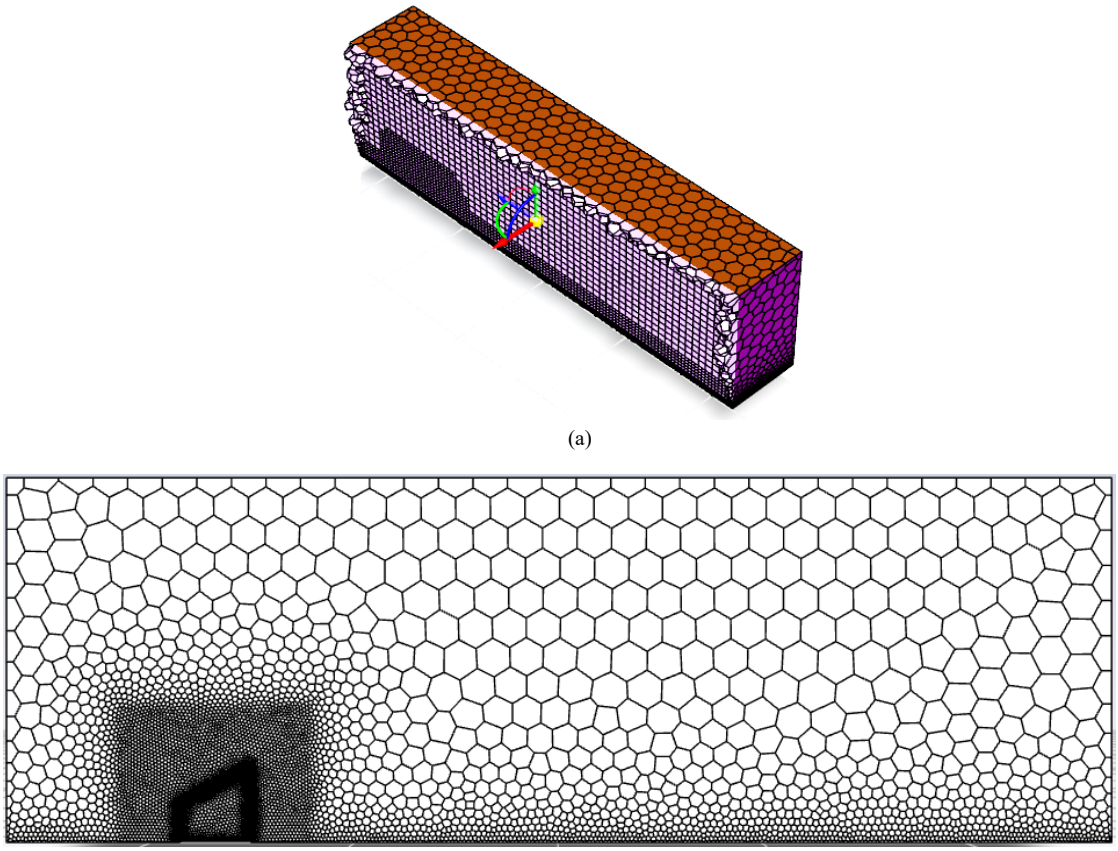

(a)

(b)

Figure 3. Poly-Hexcore of (a) volume meshing and (b) transition mesh at the building.

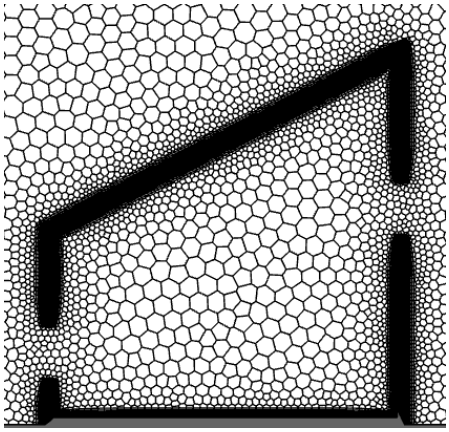

(a)

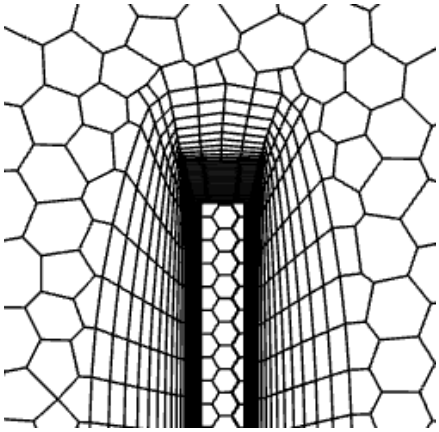

(b)

Figure 4. (a) Poly-Hexcore meshing around the building, (b) inflation layers throughout the building edges.

2.3. Boundary Conditions

Initially, throughout the wind tunnel experiment from the previous study [19], the mean wind speed and turbulence profiles were determined then it matched to a power law through a wind tunnel measurement of an amplitude of 0.25, as shown in Equation (1).

$$\left(\frac{U(z)}{U_H}\right) = \left(\frac{z}{H}\right)^{0.25} \tag{1}$$

The researchers in general believe that the logarithmic law is superior than the power law. Therefore, the logarithmic law has been employed for the velocity profile [20, 30]. Additionally, the logarithmic law was used to generate the requisite ABL frictional velocity at $0.35\ m/s$, that was needed for the turbulent dissipation rate, ε profile [31]. The aerodynamics roughness length, z_0 utilized was $0.000025\ m$, which is corresponding to $0.00005\ m$ in full scale, and thus the Von Karmann's constant, κ becomes 0.42 and z is the height coordinate, which is the building height $0.08\ m$. The corresponding inlet wind velocity profile is represented in Equation (2).

$$U(z) = \frac{u^*_{ABL}}{\kappa} ln\left(\frac{z + z_o}{z_o}\right) \tag{2}$$

Equation (3) was used to calculate the turbulent kinetic energy, k with the variability throughout the mean wind velocity and the computed turbulence intensity variations along the x, y, and z planes, whereas the I_u is the calculated streamwise turbulence intensity and 'a' is the variable with a range of 0.5 to 1.5, [22, 32]. In the current study, the parameter of 'a' used was 0.5, which is recommended from the literature [18]. Equation (4) can then be used to compute the turbulent dissipation rate, ε [31]. The specific turbulent dissipation rate, ω, in Equation (5), can be computed through the turbulent dissipation rate with the connection of using k profile as well as the empirical constant value, C_μ, which is equal to 0.09.

$$k(z) = a(Iu(z)U(z))^2 \tag{3}$$

$$\varepsilon = \frac{(u^*)^3}{\kappa(z + z_o)} \tag{4}$$

$$\omega = \frac{\varepsilon}{C_\mu k} \tag{5}$$

$$k_S = \frac{9.793\, z_0}{C_S} \tag{6}$$

The flow domain's outlet surface is identified as the pressure outlet, including zero static pressure and all standard gradients among all parameters set to zero to verify that the flow domain becomes completely generated [24, 25]. Aside from that, the domain's top and side walls were adjusted with symmetry conditions since it is normally done to ensure continuous flow. Finally, Equation (6) was used to calculate the corresponding sand-grain roughness, K_s, which employed for the surface of the flow domain's ground equal to $0.00028\ m$, and the roughness constant, C_s, was set to 0.874, which calculated depending on their relation with the aerodynamics roughness length, z_0, as founded by Blocken et al. [24]. Regarding the building surface the sand-grain roughness, K_s, value was set to zero.

2.4. Solver Settings

In the current study, the commercial CFD code along with Ansys Fluent 2021 R2 [27] was used for CFD simulations. The 3-D steady Reynolds Averaged Navier Stokes (RANS) turbulence model was chosen for this study because it provides accurate results at a lesser computational time. The SST k-ω turbulence model contains considerable differences in indoor air speed and many other distinct models as illustrated by Perén et al. [18]. Therefore, the shear stress transport, SST, k-ω model was chosen.

The pressure-based solution has been employed as the pressure velocity couplings, combined with the Semi-Implicit Method using Pressure Related Algorithms (SIMPLE) scheme. The gradients were instead calculated using the Green-Gauss node approach and second-order discretization of pressure, momentum, turbulent kinetic energy, and specific dissipation rate [20, 33]. A standard initialization scope to all zones has been used to initialize the solutions. Moreover, the solution was considered to achieve convergence when the residuals stabilize and meet a minimum value of 10^{-6} for x and z velocities, 10^{-5} for y velocity, and eventually 10^{-4} for turbulent kinetic energy, k, continuity, as well as turbulent dissipation rate, ε and specific turbulent dissipation rate, ω.

2.5. Grid Sensitivity Analysis

The shear stress transport k-ω turbulence model was used to perform a grid sensitivity analysis for the

asymmetrical opening position case (Bottom-Top). Three different grids were created to evaluate the precision of the simulation solution. The basic or medium grid (Grid B) developed has a cell count of 937,976. The coarse grid (Grid A) was created through dividing the mesh's global and local scoping size by $\sqrt{2}$, whereas the fine grid (Grid C) was created through multiplying the mesh's global and local scoping size by $\sqrt{2}$. As a result, Grids A, B, and C contains 505,974, 937,976, and 1,125,188 cells, respectively. Moreover, all the grids with their various cell counts are illustrated in Figure 5. The three grids have a same amount of inflation layers which are 10 boundary layers.

Next, the grid convergence index (GCI) established by Roache [34] has been utilized in the current study to assess the differences of the dimensionless streamwise wind speed ratio, U/U_{ref} for the coarse grid versus the medium grid and medium grid versus the fine grid. The GCI calculation is illustrated below in Equation (7), with the safety of factor (FS) set to 1.25 once three or even more grids are evaluated. The grid refinement value, r, became 2 and the formal order of accuracy, p, became 2 because of the second order finite difference technique has been applied. Five horizontal lines were created inside the building at locations of Y/H = 0.250, Y/H = 0.375, Y/H = 0.500, Y/H = 0.625 and Y/H = 0.750 and the GCI values among all three grids at these locations were averaged to obtain the GCI among each grid as represented in Table 1. It should be noted that the letter 'H' represents the building height while the letter 'Y' represents the varying height within the building. Based on the coarse grid versus the medium grid, the GCI value along the horizontal lines of Y/H = 0.250, Y/H = 0.375, Y/H = 0.500, Y/H = 0.625 and Y/H = 0.750 were 7.76% 2.22%, 1.35%, 2.00% and 3.46%, respectively. However, the basic or medium grid versus the fine grid has the GCI values of 3.75%, 2.08%, 1.47%, 1.29% and 1.66% across the horizontal lines of Y/H = 0.250, Y/H = 0.375, Y/H = 0.500, Y/H = 0.625 and Y/H = 0.750, respectively. The coarse grid has an average GCI of 3.36% whereas the medium grid has an average GCI of 2.05%. Therefore, the medium grid has been chosen for the remaining simulations because it delivers essentially grid independence outcomes and it has a lower GCI produced, which is in the acceptable range. Figure 6 shows the comparison of the U/U_{ref} values across the three grids at the locations measured which indicates that the data obtained is close to each other.

$$GCI = SF\left|\frac{r^p\,\frac{U_{coarse}-U_{fine}}{U_{ref}}}{r^p-1}\right| \tag{7}$$

$$= 1.25\left[\frac{\sqrt{2}^2\left(\frac{U_{coarse}-U_{fine}}{U_{ref}}\right)}{1-\sqrt{2}^2}\right]$$

$$= 2.5\left[\left(\frac{U_{coarse}}{U_{ref}}-\frac{U_{fine}}{U_{ref}}\right)\right]$$

Table 1. Grid convergence index (GCI) along the horizontal line for coarse grid versus medium grid and medium grid versus fine grid

Location	Grid Convergence Index (GCI)	
	Coarse versus Medium	Medium versus Fine
$Y/H = 0.250$	7.76	3.75
$Y/H = 0.375$	2.22	2.08
$Y/H = 0.500$	1.35	1.47
$Y/H = 0.625$	2.00	1.29
$Y/H = 0.750$	3.46	1.66
Average	**3.36**	**2.05**

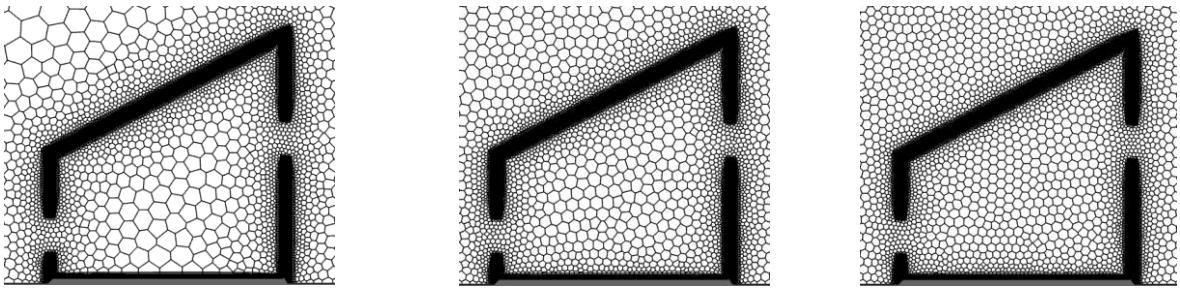

(a) (b) (c)

Figure 5. Grids in viewpoint for grid sensitivity analysis: (a) coarse grid with 505,974 cells (b) medium grid with 937,976 cells (c) fine grid with 1,125,188 cells.

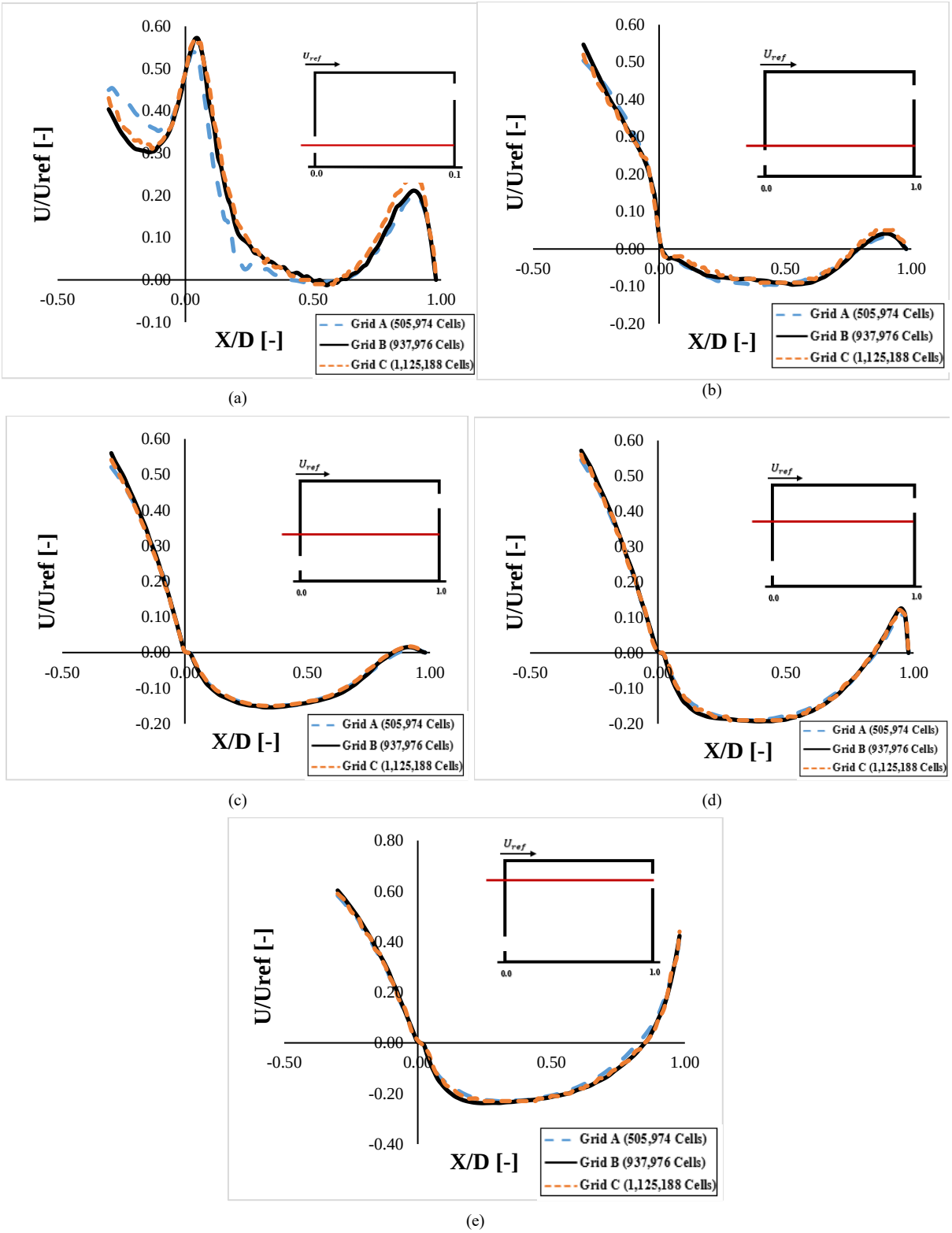

Figure 6. Grid sensitivity analysis of coarse grid (grid A), medium grid (grid B) and fine grid (grid C) for (a) $Y/H = 0.250$ (b) $Y/H = 0.375$ (c) $Y/H = 0.500$ (d) $Y/H = 0.625$ (e) $Y/H = 0.750$.

3. Simulation Cases

The sawtooth roof resembles a trapezoid design that is implemented in buildings and has a strong impact with the openings to improve the internal airflow through buildings. Table 2 shows the twelve simulation cases with sawtooth roof and various opening positions which are asymmetrical as Bottom-Top, Bottom-Middle, Middle-Top and symmetrical as Middle-Middle whereas each opening position with different roof inclination angle of 9°, 18° and 27°. The opening positions are termed based on the windward and leeward configuration. The center of the openings for the bottom, middle and top opening positions were located at $20\,mm$, $40\,mm$, and $60\,mm$ from the ground as illustrated in Figure 7. Furthermore, all windward and leeward openings have the same size of $46\,mm \times 18\,mm$ $(L \times H)$. The building model volume for all cases is 0.0008 m^3. The building windward height at roof inclination angle 9° was reduced to $72.08\,mm$ and the leeward height was increased to $87.92\,mm$ by using a trapezoid method as illustrated in Figure 7e, which is similar to the previous study by Perén at el. [18]. The building was split into half by the measurement plane to simulate the symmetry condition for the purpose of reduction in the computational time required for simulation.

Table 2. Summary of simulation cases for the sawtooth roof

Cases	Opening Position	Roof Inclination Angle	Roof Type
Case 1	Bottom-Top	9°	Sawtooth Roof
Case 2		18°	
Case 3		27°	
Case 4	Bottom-Middle	9°	
Case 5		18°	
Case 6		27°	
Case 7	Middle-Top	9°	
Case 8		18°	
Case 9		27°	
Case 10	Middle-Middle	9°	
Case 11		18°	
Case 12		27°	

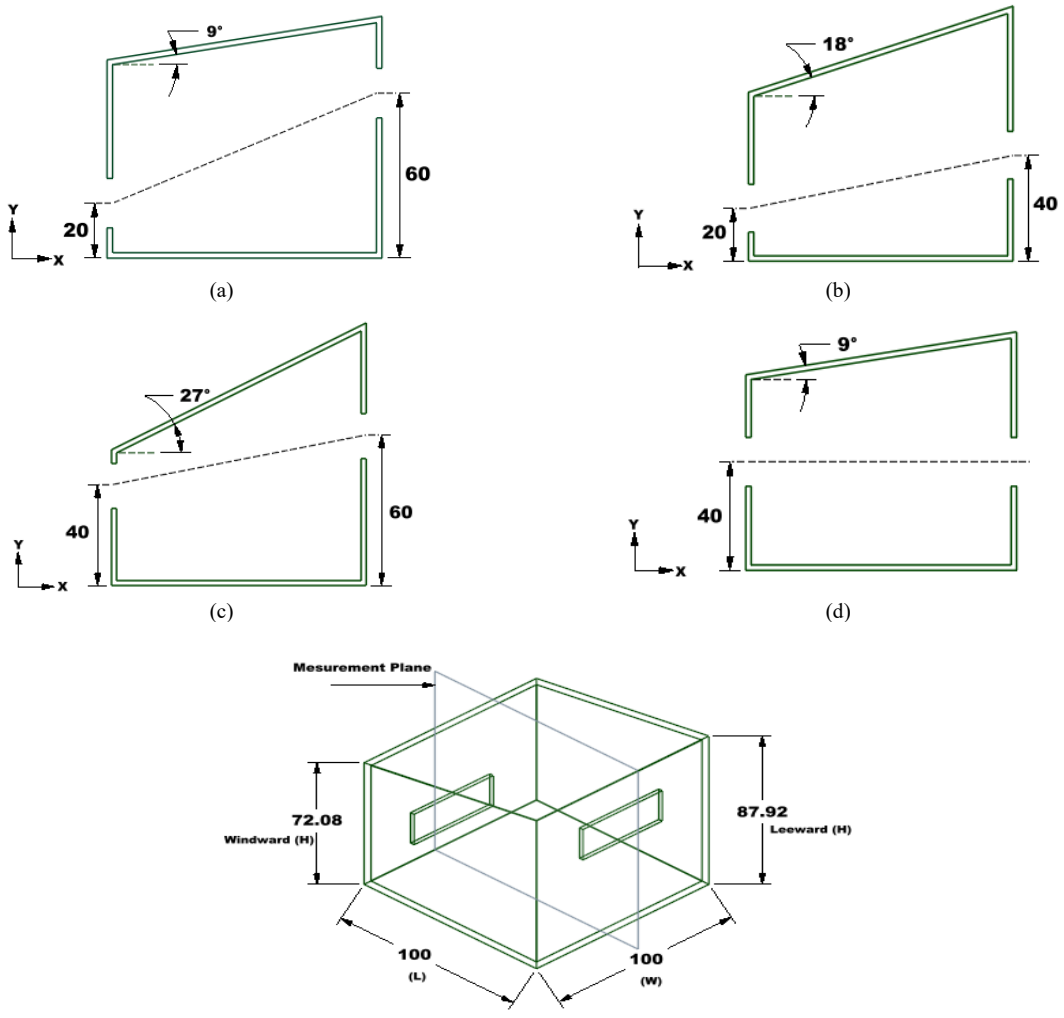

Figure 7. Opening positions with roof inclination angles (RIA) (a) bottom-top (b) bottom-middle (c) middle-top (d) middle-middle (e) RIA-9° isometric view.

4. Results and Discussion

In this section, the dimensionless velocity magnitude ($|V|/U_{ref}$), dimensionless mean streamwise velocity ratio (U/U_{ref}), pressure coefficient (Cp), contours and volume flow rate (VFR) for sawtooth roof were discussed.

4.1. Dimensionless Velocity Magnitude ($|V|/U_{ref}$)

The dimensionless velocity magnitude contours for the sawtooth roof are illustrated in Figure 8. In terms of the airflow characteristics around and inside the building model, a large area of low-magnitude velocity gradient can be seen across all opening positions whereby it is above the incoming jet. For instance, at the bottom-top and bottom-middle opening positions, it can be seen that for low roof inclination angle, the jet flow is more directed downwards which resulting in high velocity magnitude after the windward opening at 9°, whereas the higher velocity magnitude observed at the windward opening for the roof inclination angle of 27°. Next, for the middle-middle opening configuration of sawtooth roof, the inlet jet is more downward compared to the middle-top opening position. Then it can be seen that the outlet jet for the opening configurations change in direction with the changing of opening positions and increasing of roof inclination angles. Furthermore, the angle of the outlet velocity jet for bottom-top, bottom-middle and middle-middle opening positions can be seen to be angled upwards compared to middle-top opening position with roof inclination angles of 9° and 27° which are angled downward.

The peak region of the dimensionless velocity magnitude for sawtooth roof decreases and moves towards the ridge as the roof inclination angle increases to 18°. Similarly, the highest peak value of dimensionless velocity magnitude observed at roof inclination angle 9° for all opening configurations. The peak region reduces with the increases of roof inclination angles. The findings observed are in lined with the existing literature from Perén et al. [18].

The wind speed inside the building increases with the increased roof inclination angle, and the wind speed decreases when the air leaves the building. This is owing to the interdependence of air movement through the openings and the occurrence of recirculation region. The existence of the recirculation region at the bottom corner behind the building decreases gradually when the roof inclination angle increases. A significant recirculation region was noticed for the sawtooth roof, which could be attributed to the roof's sharp edge.

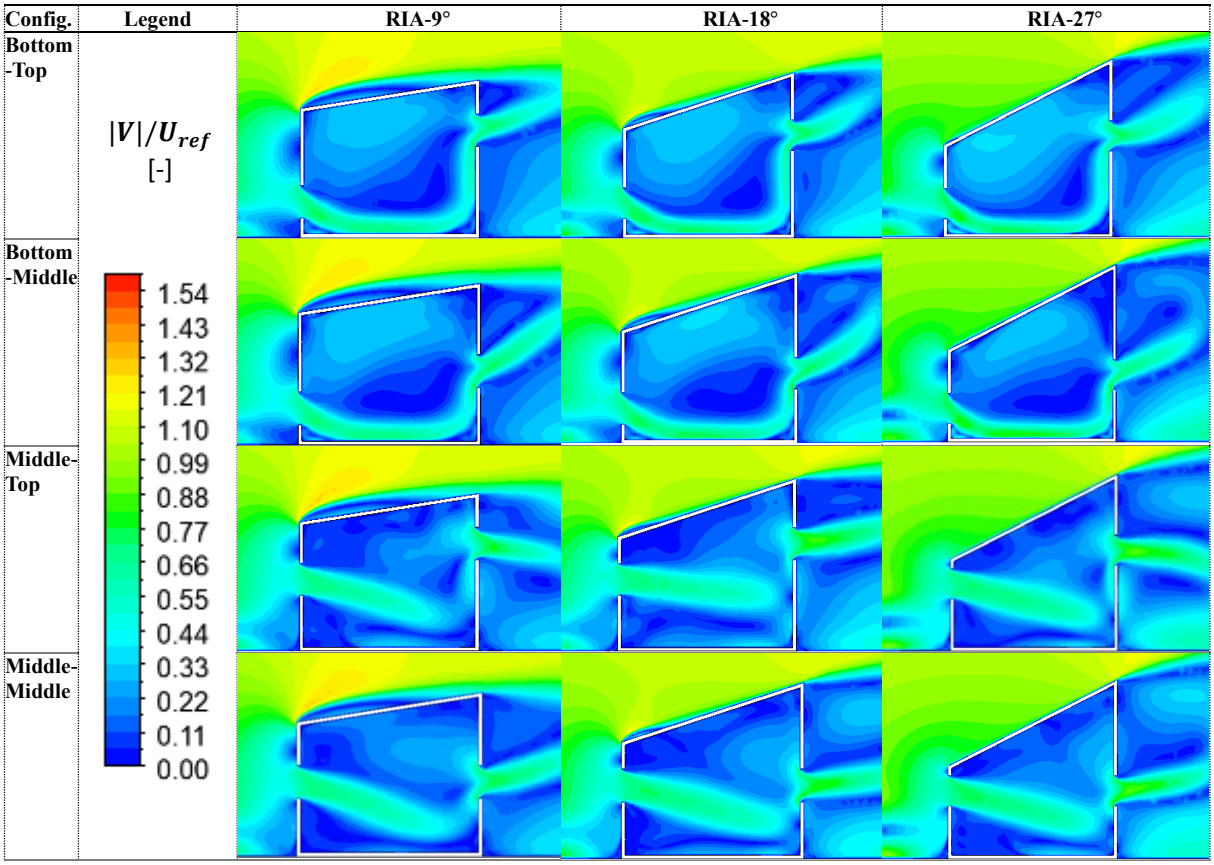

Figure 8. Contours of dimensionless velocity magnitude ($|V|/U_{ref}$) at vertical center plane.

  - Volume 16, Number 5 (ISSN 1995-6665)

4.2. Pressure Coefficient

The pressure coefficient, C_P, can be described as a non-dimensionless indication that identifies the differences between the static pressure beyond a specified fluid region and the freestream pressure as described in Equation (8). In the current study, the pressure coefficient between both the windward and leeward windows was determined. The average pressure coefficient through the windward and leeward façades was therefore subtracted to produce the difference in pressure coefficient, ΔC_P, which will be discussed in Section 4.4.

$$C_p = \frac{P - P_0}{0.5\rho {U_{ref}}^2} \tag{8}$$

The pressure coefficient contours for sawtooth roof are shown in Figure 9. The bottom-top and bottom-middle opening positions with the roof inclination angle 9° shows a high pressure gradient in the center of the building. However, it is observed that increasing the roof inclination angle up to 18° and 27° results in a low pressure within the building. In that note, the pressure increases with low inclination angles and reduced with the increased in roof inclination angles. Interestingly, the pressure coefficient contours for bottom-top opening position are in agreement with the results obtained by Perén et al. [18]. On the other hand, for the middle-top opening position, the high pressure gradient region is observed at the corner ground of leeward wall within the building for roof inclination angle of 9°. The internal high pressure gradient become lower with the increases of roof inclination angle. Furthermore, the middle-top and middle-middle opening configuration shows a higher pressure gradient within the building compared to bottom-top and bottom-middle opening configurations.

Furthermore, from all the opening configuration contours recorded, the maximum pressure in front of the building of the windward opening drops uniformly with the increase of roof inclination angle. The maximum pressure observed on the windward façade due to the influence of air colliding to the windward wall. In other words, since the varying pressure distribution mostly on the windward side, the direction of the incoming jet fluctuates slightly for each case, resulting another more horizontally directed flow as the increases of the leeward wall height and roof inclination angle. It can say that the variance in low pressure behind the building across the various scenarios is greater than the variance within high pressure in front of the building.

In overall, the roof inclination angles and opening positions has a high influence on the internal pressure within the building. Sawtooth roof shows a significantly changes in internal pressure and external observed at the windward wall. From the contours below, it can be seen that the internal and external coefficient pressure decreases with the increased of roof inclination angle. This suggests that the roof inclination angle is indeed a critical geometrical component for increasing the wind-driven cross ventilation.

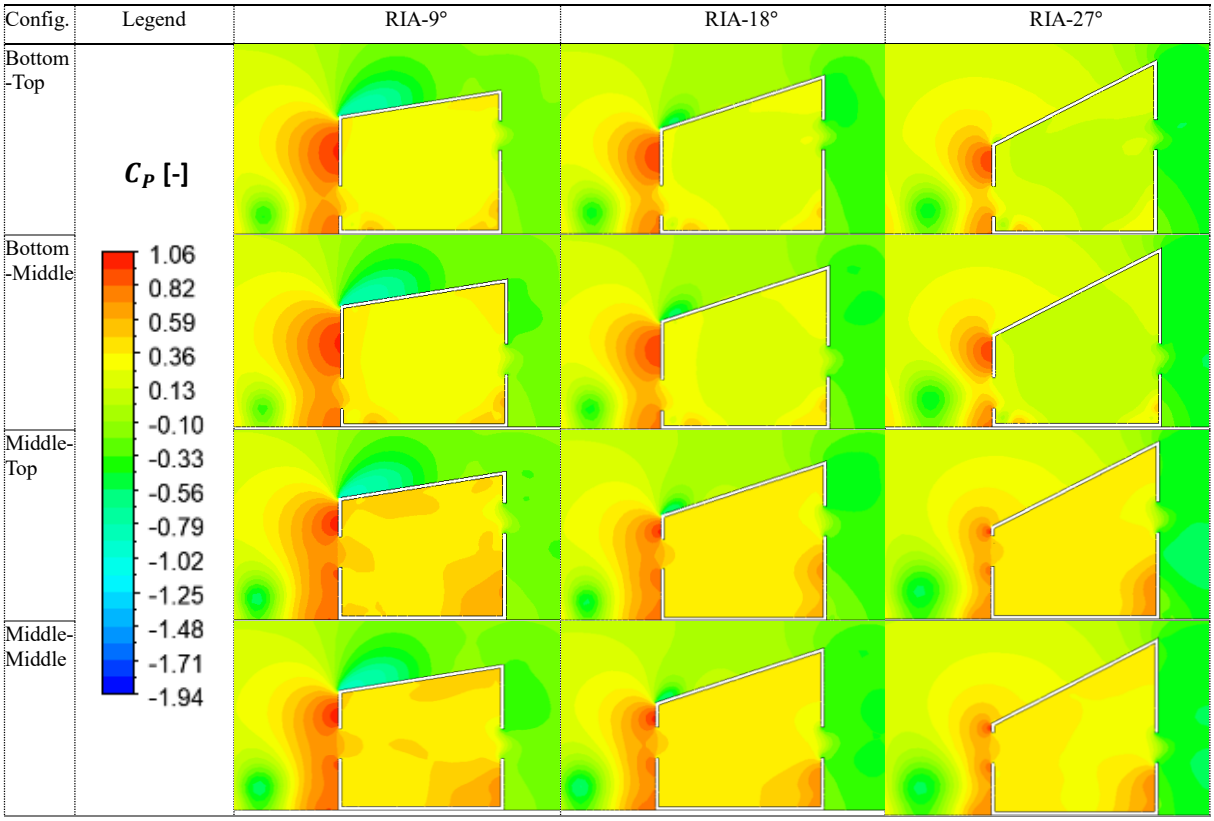

Figure 9. Contours of pressure coefficients (C_p) at vertical center plane.

4.3. Dimensionless Streamwise Wind Speed Ratio (U/U_{ref})

The velocity magnitude recorded within the building was divided by the reference velocity (U_{ref}) of 6.97 m/s at building height to make the variable obtained to be dimensionless. Thus, the resulting dimensionless streamwise wind speed ratio (U/U_{ref}) along the horizontal line were shown in Figure 10. The purpose of determine the dimensionless streamwise velocity along the horizontal line is to observe the influence of the roof inclination angles together with the impact of opening positions on the indoor airflow within the building.

For the bottom-top configuration, as the roof inclination angle increases, the streamwise wind velocity ratio increases along approximately the entire horizontal line. The indoor mean streamwise wind speed ratio along the horizontal line shows a difference in roof inclination angles, mostly between x/D of 0.1 and 0.9. Note that although the roof inclination angle of 9° has a lower streamwise wind speed ratio than the reference case (flat roof), the indoor air velocity along the horizontal line was higher in some regions observed between 0.4 < x/D < 0.6 compared to the reference case. Furthermore, for the bottom-middle configuration, it can be seen that the streamwise velocity ratio shows a small difference among the roof inclination angles, especially from 0.2 < x/D < 0.8, whereas the streamwise wind speed ratio for roof inclination angle of 27° was shifted to the left from the other roof inclination angles, between 0.1 < x/D < 0.3, despite the fact that a steeper decline of the indoor airflow compared to the bottom-top opening position. This is due to the leeward opening at the middle position that increase the resistance of the indoor air flow. On the other hand, middle-top opening position shows an increasing in streamwise wind speed ratio with increases of roof inclination angles between 0 < x/D < 0.1. The same trend is shown for the middle-middle opening positions, which clearly indicate that the streamwise wind speed ratio increases with the increasing of roof inclination angle.

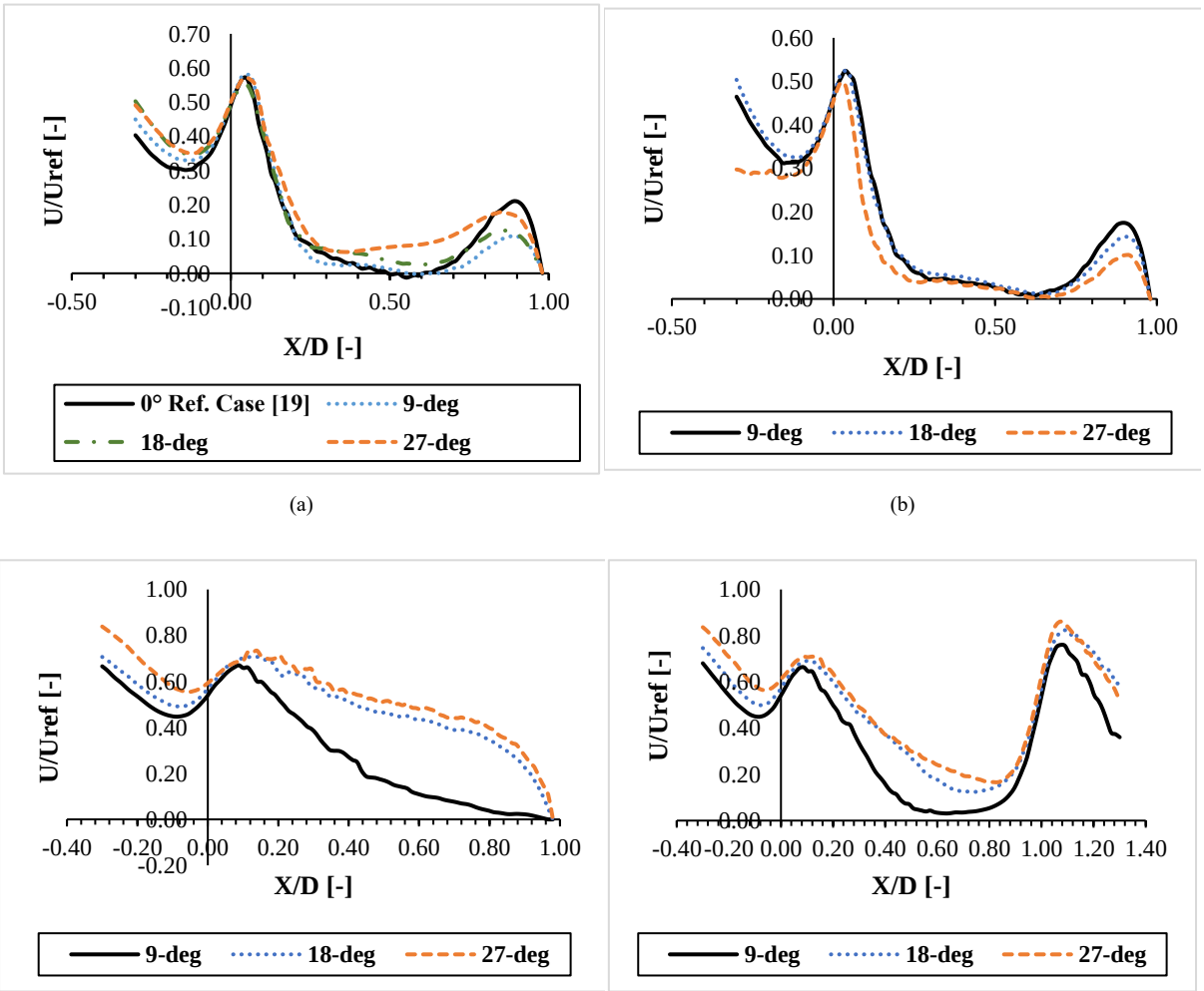

Figure 10. Dimensionless mean streamwise velocity ratio along the horizontal line for (a) bottom-top (b) bottom-middle (c) middle-top (d) middle-middle opening position.

4.4. Volume Flow Rate (VFR)

Overall volume flow rate was obtained using the following equations by Andy Walker [35]. The pressure difference, ΔC_P was calculated using the average pressure coefficients at both the windward and leeward façade, as shown in Equation (9).

$$\Delta C_p = C_{P.windward} - C_{P.leeward} \quad (9)$$

The flow coefficient, CQ was calculated using Equation (10) with the reference wind speed of 6.97 m/s and the discharge coefficient, C_D of 0.62 [36].

$$CQ = U_{ref} C_D \sqrt{\Delta C_P} \quad (10)$$

Furthermore, the flow coefficient, CQ was applied to Equation (11) to calculate the actual flow coefficient, C_a. The volume flow rate, Q was determined by using Equation (12) with the reference velocity, U_{ref} and the area of the openings, A_e of 0.000828 m^2.

$$C_a = \frac{CQ}{1 + CQ} \quad (11)$$

$$Q = U_{ref} A_e C_a \quad (12)$$

To the best of authors' knowledge, the effect of sawtooth roof inclination angles of 9°, 18° and 27° together with symmetrical and asymmetrical opening configurations was not taken into account in the literature. Hence, in the current study, the volume flow rate was used to quantify the effects of increased roof angles and change in the position of openings on the volume flow rate.

The volume flow rate for all roof inclination angles of 9°, 18° and 27° along with the opening configurations were shown in Figure 11. It can be seen that the volume flow rate increases with the increase in roof inclination angle from all opening configurations. It can be seen that the roof inclination angle of 27° with middle-top opening position has the highest volume flow rate of 115% and then followed by the bottom-top, middle-middle and bottom-middle opening positions with the volume flow rate of 109%, 108% and 106%, respectively. This differences between the highest and the lowest volume flow rate is due to the pressure differences across the windward and leeward openings. However, it should be mentioned that the roof angle of 27° is the geometry with the largest leeward height. The building height can be another factor that influences the volume flow rate. These findings are in line with the existing literature of the asymmetrical opening position by Perén which discovered that the increased of roof inclination angles more than 18° compared to the refrence case (Flat roof) can increase the volume flow rate [18]. Furthermore, among all the three-inclination angles for the middle-top opening position can be seen only a slight difference in volume flow rate up to 0.68% which indicate in a better volume flow rate through the building for the middle-top opening position regardless of the roof inclination angles.

Next, the bottom-top opening position has a significant increase in volume flow rate of 5% from the roof inclination angle of 9° to 18° and 9% from the roof inclination angle of 18° to 27°. On the other hand, the bottom-middle opening configuration has the lowest volume flow rate from roof inclination angle of 27° at 106% while the roof inclination angles of 9° and 18° indicate a higher volume flow rate with 103% and 105% compared to bottom-top and middle-middle configurations. Additionally, the volume flow rate for middile-middle opening configuration increased by 3% from the roof inclination angle of 9° to 18° and 4% from the roof inclination angle of 18° to 27°. Increasing the roof inclination angle can increase the volume flow rate. The middle-middle opening position along with the roof inclination angles are in line with the previous study by Kindangen [37], which discovered that increasing of roof inclination angle has a significant impact on the volume flow rate inside the building.

In overall, higher volume flow rate was observed when the leeward opening located near the roof and the windward opening located at the middle. On the other hand, the building experienced weaker volume flow rate when the windward openings located near the ground. Nevertheless, changing the windward opening to a higher position near the roof can potentially increase the volume flow rate with the increases of roof inclination angles within the building [38].

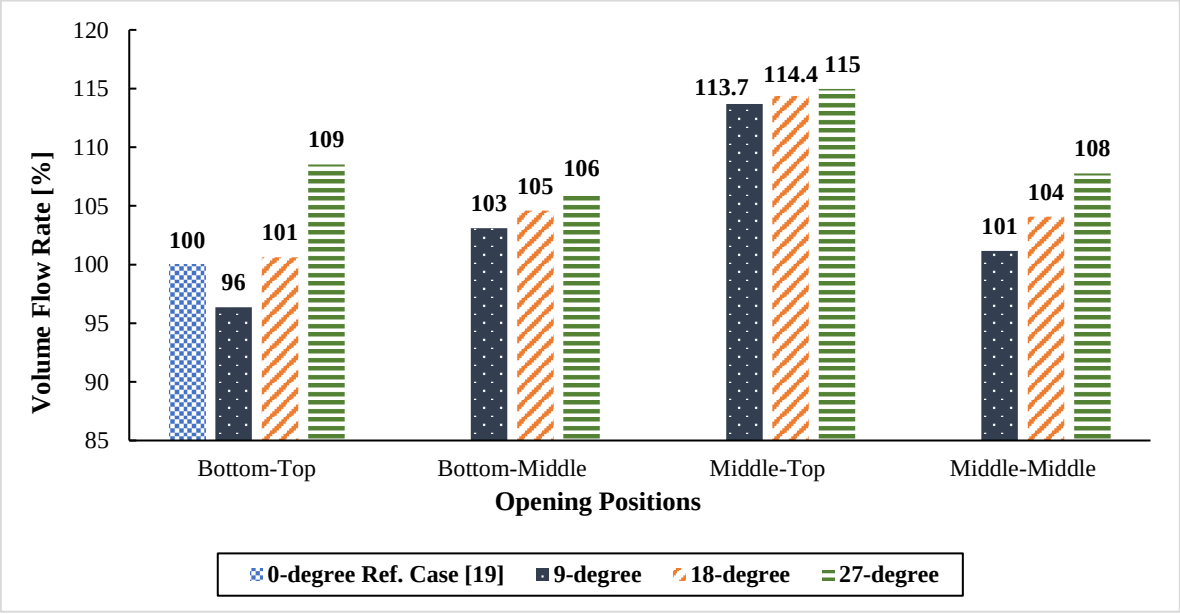

Figure 11. Impact of roof inclination angle (RIA) and opening positions on volume flow rate (VFR)

5. Conclusion

The influence of sawtooth roof together with the opening positions and various roof inclination angles have been analysed. The roof inclination angles considered are 9°, 18° and 27° whereas the opening positions considered are bottom-top, bottom-middle, middle-top and middle-middle. These opening configurations mentioned were based on the windward and leeward positions. The computational domain was designed based on the recommendations and current practices for natural ventilation provided in the literature [20-23]. Grid convergence index (GCI) analysis was carried out and GCI average of less than 3% was achieved, which is within the acceptable range. The medium grid (Grid B) was chosen with the shear stress transport k-ω turbulence model for the subsequent simulation cases as it has a good agreement with a reference case from the literature [19]. The results from the simulations were analysed in terms of the dimensionless velocity magnitude, pressure coefficient, dimensionless streamwise wind speed ratio and volume flow rate collectively. The main findings from this study can be summarized as below:

- The speed of the airflow throughout the building is influenced by the recirculation region and internal stagnation point.
- Opening closer to the roof of the building generates a higher volume flow rate through the building regardless of the roof inclination angles used. Similarly, the highest volume flow rate obtained in the simulations was 115% from middle-top opening position with the roof inclination angle 27°. The findings were in lined with the findings from the existing literature [18].
- To enhance the volume flow rate (VFR) inside the low-rise building, the roof inclination angle should be greater than 18°, whereas lower roof inclination angle like 9°, results in a lower volume flow rate (VFR) compared to reference case building (flat roof).
- Pressure coefficient recorded was higher for the middle-top opening position and roof inclination angle 9° compared to middle-middle opening position across all roof configurations. This can be attributed to the added flow resistance by the difference in the position of the windward and leeward openings. Meanwhile, the bottom-top opening position recorded a lower pressure coefficient compared to the bottom-middle opening position.

Overall, it can be concluded that the current study has provided significant findings which can be considered novel in the field of natural ventilation as there are not many studies involving cross ventilation and roof inclination angle with opening positions concurrently and the implications of the volume flow rate, pressure coefficient and airflow pattern for the natural ventilated building. Nonetheless, further study can be done to assess the impact of roof configuration design parameters for the building ventilation performance.

6. Future Recommendation

The current study was an investigation on the natural ventilation of isolated building with limitations. However, some improvements can be included in future work for better and broader research. Therefore, the future work can follow the below aspects:

- This research intents on the wind angle of 0°. The ventilation performance can be possibly changed for various wind angles.
- In the current research, all the simulations obtained for isothermal condition. Future work can focus on non-isothermal condition to analyse the impact of temperature gradients within the building, the balance across wind and buoyancy such as driving forces of the ventilation flow and better understanding the heat transfer within the building.
- In the current study, only the sawtooth roof with three roof inclination angles were considered which are 9°, 18°, and 27°. Future work different roof configurations and higher roof inclination angles can be considered to possibly increase the ventilation performance for the building.
- The impact of obstacles inside the building at different positions with the presence of roof configuration.

References

[1] C.H. Lim, O. Saadatian, K. Sopian, M.Y. Sulaiman, S. Mat, E. Salleh, “Design configurations analysis of wind-induced natural ventilation tower in hot humid climate using computational fluid dynamics”. International Journal of Low-Carbon Technologies, Vol. 10, No. 4, 2013, 332-346.

[2] M.N. Khan, I. Janajreh, “Transevaporative cooling performance of a three-sided wind catcher”. Jordan Journal of Mechanical and Industrial Engineering, Vol. 11, No. 4, 2017, 225-233.

[3] Yong M, Lesjak M, Hor K, Rowse B, Tandon S. Compendium of policy and financial instruments for accelerating building sector energy efficiency in Malaysia. Kuala Lumpur: Building Sector Energy Efficiency Project (BSEEP); 2017.

[4] N.A. Hassan, Z. Hashim, J.H. Hashim, “Impact of climate change on air quality and public health in urban areas”. Asia Pacific Journal of Public Health, Vol. 28, No. 2, 2014, 38-48.

[5] N.C. Kar, L.K. Moey, T.F. Go, P.L. Chong, and C.M. Chia, “Short review on renewable energy policy and energy consumption of buldings in Malaysia”. International Journal of Engineering and Advanced Technology, Vol. 7, No. 1, 2022, 64-82.

[6] R. Behari, “Special Report: Almost out of time | The Edge Markets,” The Edge Malaysia, 2020. https://www.theedgemarkets.com/article/special-report-almost-out-time (Accessed 2 June 2022).

[7] S.A. Ahmed, H.O. Mahammed, “A statistical analysis of wind power density based on the weibull and ralyeigh models of "Penjwen region" Sulaimani/Iraq”. Jordan Journal of Mechanical and Industrial Engineering, Vol. 6, No. 2, 2012, 135-140.

[8] N. Hussein, “Greenhouse gas emissions reduction potential of Jordan’s utility scale wind and solar projects”. Jordan Journal of Mechanical and Industrial Engineering, Vol. 10, No. 3, 2016, 199-203.

[9] L.K. Moey, M.F. Kong, V.C. Tai, T.F. Go, N.M. Adam, “Effect of gable roof angle on natural ventilation for an isolated building”. Jordan Journal of Mechanical and Industrial Engineering, Vol. 15, No. 3, 2021, 291-300.

[10] C.H. Lim, O. Saadatian, M.Y. Sulaiman, S. Mat, K. Sopian, M.R. Mahyuddin, K.C. Ng, “Using computational fluid dynamics (CFD) method in analyzing different design configurations of Venturi-shaped wind-induced natural ventilation towers”. Latest trends in renewable energy and

environmental informatics : proceedings of the 4th international conference on renewable energy sources (RES '13), proceedings of the 1st international conference on environmental informatics (ENINF '13) : Kuala Lumpur, Malaysia, 2013.

[11] L. K. Moey, N. M. Adam, K. A. Ahmad, "Effect of venturi-shaped roof angle on air change rate of a stairwell in tropical climate". Journal of Mechanical Engineering., Vol. 4, No. 4, 2017, 135-150.

[12] L.K. Moey, M.F. Kong, V.C. Tai, T.F. Go, N.M. Adam, "Effects of roof configuration on natural ventilation for an isolated building". Journal of Mechanical Engineering Science, Vol. 15, No. 3, 2021, 8379-8389.

[13] Y. Tominaga, S.I. Akabayashi, T. Kitahara, Y. Arinami, "Air flow around isolated gable-roof buildings with different roof pitches: Wind tunnel experiments and CFD simulations". Building and Environment, Vol. 84, No. 1, 2015, pp. 204-213.

[14] Z. Liu, Z. Yu, X. Chen, R. Cao, F. Zhu, "An investigation on external airflow around low-rise building with various roof types: PIV measurements and LES simulations". Building and Environment, Vol. 169, No. 2, 2020, 106-583.

[15] J.I. Perén, T.V. Hooff, B.C.C. Leite, B. Blocken, "CFD simulation of wind-driven upward cross ventilation and its enhancement in long buildings: Impact of single-span versus double-span leeward sawtooth roof and opening ratio". Building and Environment, Vol. 96, No. 4, 2015, 142-156.

[16] M.A. Lukiantchuki, R. Caram, E. Matsumoto, L.C. Labaki, "Natural Ventilation by Air Captors and Extractors Sheds in Hospitals in Brazil: Wind Tunnel Measurements". Journal of Civil Engineering and Architecture, Vol. 8, No. 10, 2014, 1293-1303.

[17] N.S. Fouad, G.H. Mahmoud, N.E. Nasr, "Comparative study of international codes wind loads and CFD results for low rise buildings". Alexandria Engineering Journal, Vol. 57, No. 4, 2018, 3623-3639.

[18] J.I. Perén, T.V. Hooff, B.C.C. Leite, B. Blocken, "CFD analysis of cross-ventilation of a generic isolated building with asymmetric opening positions: Impact of roof angle and opening location". Building and Environment, Vol. 85, No. 2, 2015, 263-276.

[19] P. Karava, T. Stathopoulos, A.K. Athienitis, "Airflow assessment in cross-ventilated buildings with operable façade elements". Building and Environment, Vol. 46, No. 1, 2011, 266-279.

[20] R. Ramponi, B. Blocken, "CFD Simulation of cross-ventilation for a generic isolated building: impact of computational parameters". Building and Environment, Vol. 53, 2012, 34-48.

[21] J. Franke, A. Hellsten, H. Schlunzen, B. Carissimo, Best practice guideline for the CFD simulation of flows in the urban environment, 1st ed. Belgium: Cost Action; 2007.

[22] Y. Tominaga, A. Mochida, R. Yoshie, H. Kataoka, T. Shirasawa, "AIJ guidelines for practical applications of CFD to pedestrian wind environment around buildings". Journal of Wind Engineering and Industrial Aerodynamics, Vol. 96, No. 10-11, 2008, 1749-1761.

[23] R. Ramponi, B. Blocken, "CFD simulation of cross-ventilation flow for different isolated building configurations: Validation with wind tunnel measurements and analysis of physical and numerical diffusion effects". Journal of Wind Engineering and Industrial Aerodynamics, Vol. 104–106, 2012, 408-418.

[24] B. Blocken, T. Stathopoulos, J. Carmeliet, "CFD simulation of the atmospheric boundary layer: wall function problems." Atmospheric Environment, Vol. 41, No. 2, 2007, 238-252.

[25] B. Blocken, J. Carmeliet, T. Stathopoulos, "CFD evaluation of wind speed conditions in passages between parallel buildings - Effect of wall-function roughness modifications for the atmospheric boundary layer flow". Journal of Wind Engineering and Industrial Aerodynamics, Vol. 95, No. 9–11, 2007, 941-962.

[26] T. Kolev, P. Fischer, M. Min, J. Dongarra, "Efficient exascale discretizations: High-order finite element methods". International Journal of High Performance Computing Applications, Vol. 35, No. 6, 2021, 527-552.

[27] ANSYS, "Ansys Fluent 2021 R2 Theory Guide," 2021. [Online]. Available: https://www.ansys.com/content/dam/campaigns/abm/technip/fluent-workflows.pdf [Accessed 17 October 2021]

[28] K. Zore, B. Sasanapuri, G. Parkhi, A. Varghese, "ANSYS mosaic Poly-Hexcore mesh for high-lift aircraft configurations". 21st AeSI Annual CFD Symposium, Bangalore, India, 2019.

[29] Alawadhi EM. Finite Element Simulations Using ANSYS, Boca Raton: CRC Press; 2015

[30] M. Shirzadi, P.A. Mirzaei, M. Naghashzadegan, Y. Tominaga, "Modelling enhancement of cross-ventilation in sheltered buildings using stochastic optimization". International Journal of Heat and Mass Transfer, Vol. 118, 2018, 758-772.

[31] P.J. Richards R.P. Hoxey, "Appropriate boundary conditions for computational wind engineering models using the k-ϵ turbulence model". Journal of Wind Engineering and Industrial Aerodynamics, Vol. 46–47, No. 8, 1993, 145-153.

[32] P. Karava, T. Stathopoulos, A.K. Athienitis, "Wind-induced natural ventilation analysis". Solar Energy, Vol. 81, No. 1, 2007, 20-30.

[33] T. van Hooff, B. Blocken, Y. Tominaga, "On the accuracy of CFD simulations of cross-ventilation flows for a generic isolated building: Comparison of RANS, LES and experiments". Building and Environment, Vol. 114, 2017, 148-165.

[34] P.J. Roache, "Quantification of uncertainty in computational fluid dynamics". Annual Review of Fluid Mechanics, Vol. 29, No. 1, 1997, 123-160.

[35] A. Walker, "Natural Ventilation.," Whole Building Design Guide [Online], 2016. https://www.wbdg.org/resources/natural-ventilation?r=env_wall (Accessed 17 October 2021).

[36] C.R. Chu, Y.H. Chiu, Y.J. Chen, Y.W. Wang, C.P. Chou, "Turbulence effects on the discharge coefficient and mean flow rate of wind-driven cross-ventilation". Building and Environment, Vol. 44, No. 10, 2009, 2064-2072.

[37] J. Kindangen, G. Krauss, P. Depecker, "Effects of roof shapes on wind-induced air motion inside buildings". Building and Environment, Vol. 32, No. 1, 1997, 1-11.

[38] N.F.M. Kasim, S.A. Zaki, M.S.M. Ali, N. Ikegaya, A.A. Razak, "Computational study on the influence of different opening position on wind-induced natural ventilation in urban building of cubical array". Procedia Engineering, Vol. 169, 2016, 256-263.